

## Supporting information

### High-Performance Self-Powered Solar-Blind UV Photodetector

#### Based on Annealed $\text{Sc}_{0.74}\text{In}_{1.26}\text{O}_3$ Ternary Alloy Film

*Zhengdong Jiang,<sup>a</sup> Peicheng Jiao,<sup>a</sup> Yutao Xiong,<sup>a</sup> Zhiyuan Luo,<sup>a</sup> Dan Zhang,<sup>b</sup>*

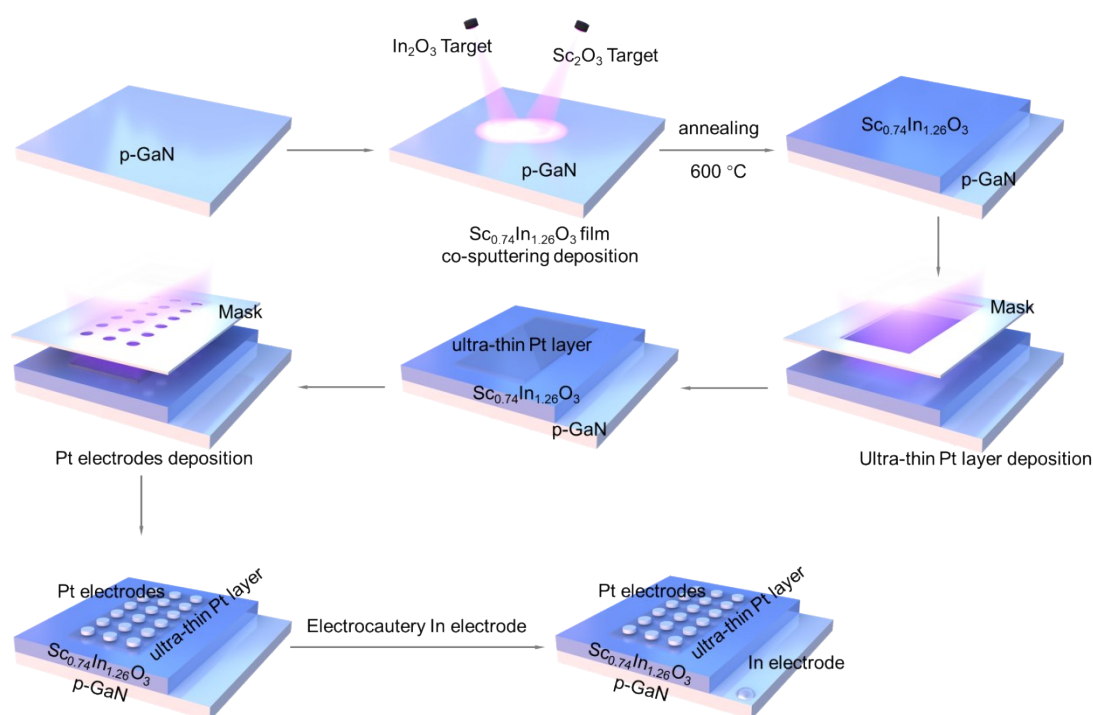
*Yanghui Liu<sup>\*a</sup> and Wei Zheng<sup>a</sup>*

<sup>a</sup> School of Materials, Shenzhen Campus of Sun Yat-sen University, Sun Yat-Sen University, Shenzhen 518107, China

<sup>b</sup> the School of Physics and Optoelectronic Engineering, Guangdong University of Technology, Guangzhou 510006, China.

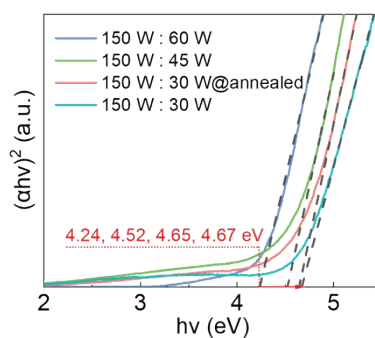
Email for corresponding authors : [liuyanghui@mail.sysu.edu.cn](mailto:liuyanghui@mail.sysu.edu.cn)

Figure S1 illustrates the preparation process of the  $\text{Sc}_{0.74}\text{In}_{1.26}\text{O}_3$  film and the construction process of the SBUV photodetector based on it. Initially, using high-purity  $\text{Sc}_2\text{O}_3$  (purity 99.99%) and  $\text{In}_2\text{O}_3$  (purity 99.99%) targets as the Sc and In sources, respectively, a ternary alloy thin film of  $\text{Sc}_{0.74}\text{In}_{1.26}\text{O}_3$  was deposited on a clean p-GaN substrate via magnetron co-sputtering. After deposition, the film was annealed in air at  $600^\circ\text{C}$  for 1 hour. Subsequently, an ultrathin Pt layer was sputtered onto the  $\text{Sc}_{0.74}\text{In}_{1.26}\text{O}_3$  film surface through a mask to serve as a collection window for photogenerated carriers. On this basis, Pt metal electrodes were further sputtered to form ohmic contacts. Finally, the bottom In electrode was connected to the p-GaN substrate by electrocautery, completing the device fabrication.



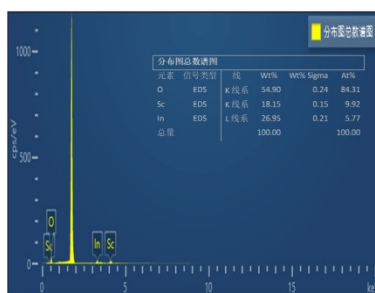
**Figure S1.** Schematic illustration of the preparation of the  $\text{Sc}_{0.74}\text{In}_{1.26}\text{O}_3$  film and the fabrication process of the SBUV photodetector based on it.

By fixing the sputtering power of the  $\text{Sc}_2\text{O}_3$  target at 150 W and adjusting the sputtering power of the  $\text{In}_2\text{O}_3$  target to 30 W, 45 W, and 60 W,  $\text{Sc}_x\text{In}_{2-x}\text{O}_3$  ternary alloy films with different Sc and In composition ratios were successfully fabricated. The bandgaps of the films with various compositions are shown in Figure S2.



**Figure S2.** Bandgaps of  $\text{Sc}_x\text{In}_{2-x}\text{O}_3$  thin films obtained under different sputtering powers of  $\text{In}_2\text{O}_3$  target.

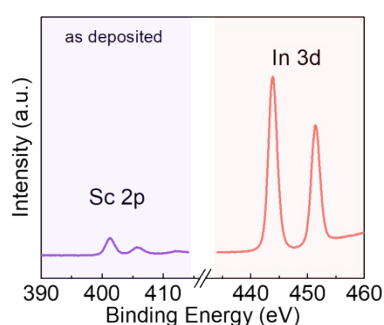
Figure S3 presents the EDS analysis results of the  $\text{Sc}_x\text{In}_{2-x}\text{O}_3$  film prepared under a sputtering power of 30 W for the  $\text{In}_2\text{O}_3$  target. Through quantitative analysis of the EDS spectrum, the atomic ratio of Sc to In was calculated to be 1:1.7, indicating that the chemical composition of the film can be precisely represented as  $\text{Sc}_{0.74}\text{In}_{1.26}\text{O}_3$ .



**Figure S3.** EDS spectrum of the  $\text{Sc}_{0.74}\text{In}_{1.26}\text{O}_3$  film.

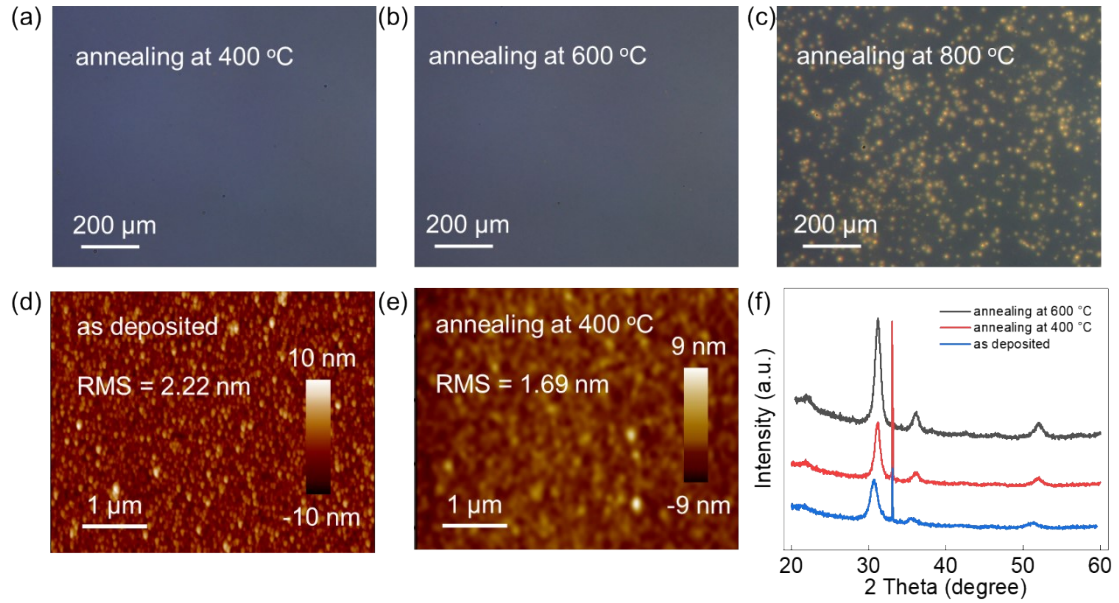
Figure S4 presents the high-resolution XPS spectra of Sc 2p and In 3d for the  $\text{Sc}_{0.74}\text{In}_{1.26}\text{O}_3$  thin film before annealing. Through quantitative analysis of the spectra,

the atomic ratio of In/Sc was calculated to be 2.4. Compared with the atomic ratio of In/Sc in the annealed  $\text{Sc}_{0.74}\text{In}_{1.26}\text{O}_3$  thin film (2.3), the difference is minimal, indicating that the composition ratio of Sc and In in the film remains essentially unchanged before and after annealing. This result further confirms that the annealing process has a limited impact on the chemical stability of the film.



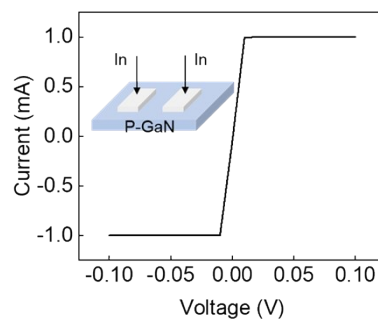
**Figure S4.** High-resolution XPS spectra of Sc 2p and In 3d for the  $\text{Sc}_{0.74}\text{In}_{1.26}\text{O}_3$  thin film before annealing.

Figure S5 presents the systematic rationale for selecting this specific annealing temperature. Judging from the optical images in Figure S5 (a-c), the films annealed at 400 °C and 600 °C have good quality, while the films annealed at 800 °C show a large number of holes. In addition, the AFM images in Figures S5 (d-e) and Figure 1 (f) show that the mean square roughness of the films before annealing, annealed at 400 °C and 600 °C is 2.22 nm, 1.69nm and 1.58nm, respectively, indicating that the films annealed at 600 °C have the smoothest surface. Furthermore, the XRD results of Figure S5 (f) indicate that the film annealed at 600 °C has a better crystallinity. Based on the above analysis, we believe that 600°C is the optimal annealing temperature.



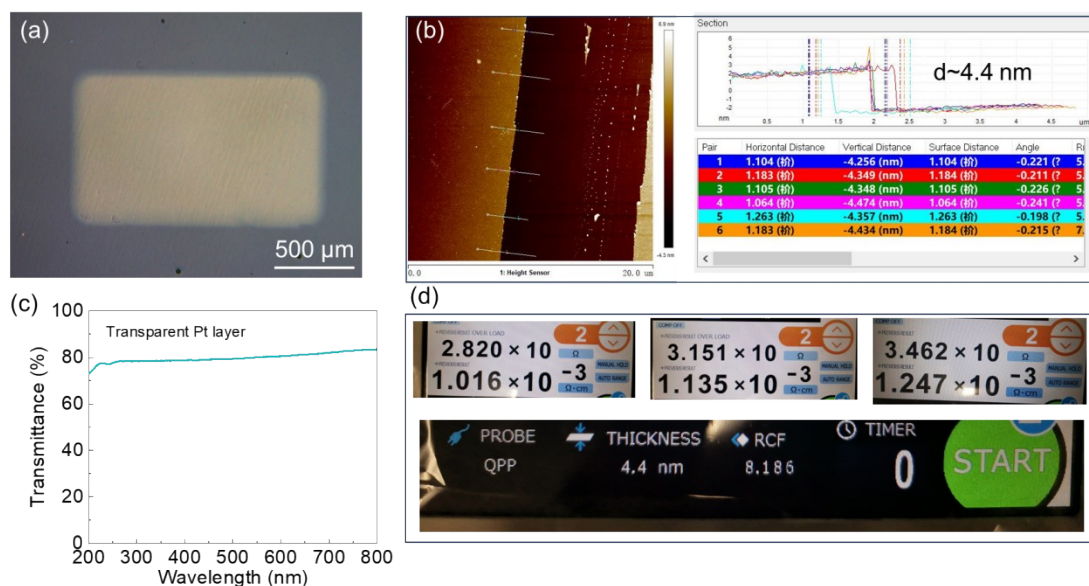
**Figure S5.** Optical images of  $\text{Sc}_{0.74}\text{In}_{1.26}\text{O}_3$  films annealed at (a) 400 °C, (b) 600 °C, and (c) 800 °C. AFM image of  $\text{Sc}_{0.74}\text{In}_{1.26}\text{O}_3$  thin films (d) before annealing, (e) annealed at 400 °C. (f) XRD patterns of the  $\text{Sc}_{0.74}\text{In}_{1.26}\text{O}_3$  thin films on silicon substrates before and after annealing.

Figure S6 presents the I-V curve between In/p-GaN/In. It can be seen that there is a good ohmic contact between In and p-GaN, indicating that there is no energy barrier at the In and p-GaN interface.



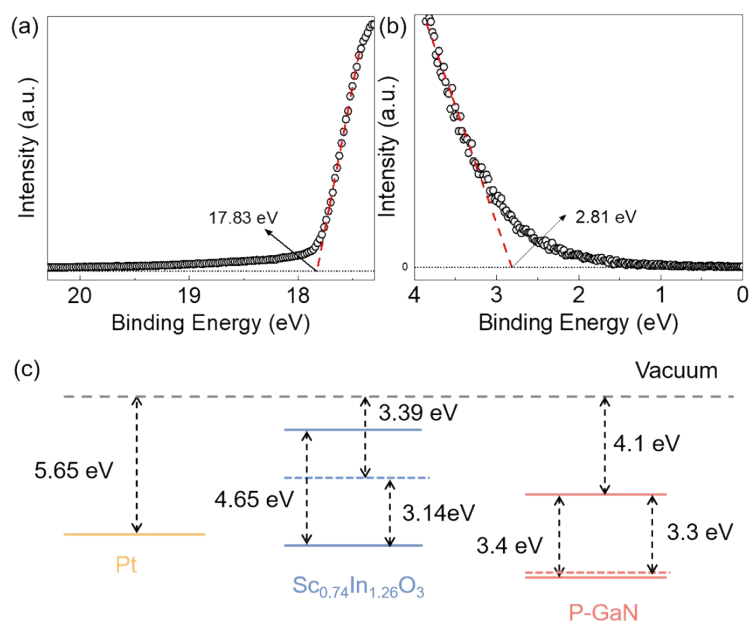
**Figure S6.** I-V curve of In/p-GaN/In.

Figure S7 provides a systematic characterization of the thickness, optical, and electrical properties of the ultrathin Pt layer. Figure S7(a) shows the optical microscope image of the ultrathin Pt layer, with geometric dimensions of 1.5 mm in length and 0.75 mm in width, corresponding to an area of approximately 1.125 mm<sup>2</sup>. Figure S7(b) presents the AFM image of the ultrathin Pt film. By randomly selecting six step measurement positions (indicated by the white dashed lines) and analyzing the corresponding step height profiles (shown on the right of Figure S7(b)), the thickness of the ultrathin Pt layer is determined to be approximately 4.4 nm. Figure S7(c) displays the UV-Vis transmission spectrum of the ultrathin Pt layer deposited on a quartz substrate, showing a high transmittance of about 80% in the wavelength range of 200-800 nm. Figure S7(d) further illustrates the resistivity test results of the ultrathin Pt layer, with a value of  $1.133 \pm 0.116 \times 10^{-5} \Omega \cdot \text{m}$ , confirming its excellent electrical conductivity. Collectively, these results indicate that the ultrathin Pt layer can effectively serve as an electron collection window while maintaining high transmittance and without significantly affecting the absorption characteristics of the  $\text{Sc}_{0.74}\text{In}_{1.26}\text{O}_3$  photosensitive layer for SBUV.



**Figure S7.** (a) Image of the ultrathin Pt layer under optical microscopy; (b) AFM image of the ultrathin Pt film, with white dashed lines indicating the selected step measurement positions, and the right figure showing the step height profile of the ultrathin Pt layer, with a thickness of approximately 4.4 nm; (c) Transmission spectrum of the ultrathin Pt layer; (d) Resistivity test data image of the ultrathin Pt layer.

The work function of  $\text{Sc}_{0.74}\text{In}_{1.26}\text{O}_3$  and the energy difference between the Fermi level and the valence band maximum (VBM) were determined by UPS measurements. As shown in Figures S8 (a) and (b), these values were calculated to be 3.39 eV (from 21.22 eV – 17.83 eV) and 2.81 eV, respectively. Based on the above information and the band gaps data extracted from Figure 1 (a), we obtained a more accurate band diagram of  $\text{Sc}_{0.74}\text{In}_{1.26}\text{O}_3$ . Figure S8 (c) shows the energy band structure of isolated Pt,  $\text{Sc}_{0.74}\text{In}_{1.26}\text{O}_3$  and p-GaN. Upon intimate contact between these components, their Fermi levels align to reach equilibrium, resulting in band bending at the material interfaces, as shown in Figure 2 (b).



**Figure S8.** UPS characterization of  $\text{Sc}_{0.74}\text{In}_{1.26}\text{O}_3$  film annealed at 600 °C. (a) Secondary electron cut-off region, (b) Valence band region, (c) Equilibrium energy band alignment diagram of isolated Pt,  $\text{Sc}_{0.74}\text{In}_{1.26}\text{O}_3$ , and p-GaN components.

Figure S9 presents the I-T curve of the SBUV photodetector without an ultrathin Pt layer, under 255 nm UV light irradiation at 23.6  $\mu\text{W}$  and 0 V bias. Comparative analysis of the performance of the SBUV photodetector with an ultrathin Pt layer reveals that the introduction of the ultrathin Pt layer significantly enhances the photoresponse performance of the device.

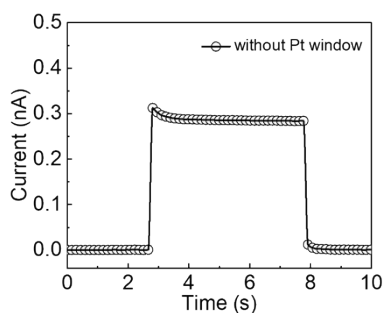


**Figure S9.** I-T curve of the SBUV photodetector without an ultrathin Pt layer under

255 nm UV light irradiation at 23.6  $\mu$ W and 0 V bias.

Figure S10 presents a comparison of the multi-cycle I-T characteristics under both ambient light and dark conditions. Notably, the device exhibits negligible variation in photocurrent between ambient light and dark environments, demonstrating robust anti-interference capability and excellent operational stability.

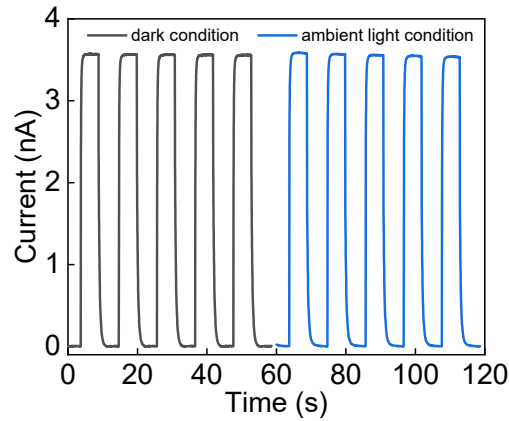


**Figure S10.** Comparison of multi-cycle I-T curves of the device under ambient light and dark conditions

Compared to recent studies on SBUV photodetectors (Refs. 1-5), our  $\text{Sc}_{0.74}\text{In}_{1.26}\text{O}_3$ -based device demonstrates superior performance in terms of dark current, spectral selectivity, and response speed, as summarized in Table 1. This advancement highlights the potential of our approach for future SBUV photodetector development.

**Table S1.** Performance comparison of SBUV photodetectors in recent years.

	bias	$R_{\text{peak}}$ (mA/W)	PDCR	$R_{\text{peak}}/R_{\text{vis}}$ ( $\times 10^3$ )	FWMH (nm)	$\tau_d$ (ms)	Reference
$\text{Lu}_{0.27}\text{Sn}_{0.73}\text{O}$	0V	$\sim 0.34@289\text{nm}$	$<10^2$	4.5	/	90.7	1

ScO <sub>x</sub>	0V	5.77@258nm	~10 <sup>3</sup>	0.589	/	182	2
Lu <sub>0.39</sub> In <sub>0.61</sub> O	0V	0.81@255nm	/	0.318	/	560	3
(Sc <sub>0.06</sub> Ga <sub>0.94</sub> ) <sub>2</sub> O <sub>3</sub>	10V	210@245nm	/	0.63	/	167	4
AlSnO	5V	400@239nm	~10 <sup>5</sup>	/	58	<1000	5
Sc <sub>0.74</sub> In <sub>1.26</sub> O <sub>3</sub>	0V	0.71@254nm	>10 <sup>3</sup>	2.45	45	261	This work

---

## Reference

- 1 D. Zhang, J. Liang, H. Cai, Z. Lin, G. Tang, X. Tang, Q. Sun and W. Zheng, *IEEE Transactions on Electron Devices*, 2024, **71**, 2491–2496.
- 2 F. Li, J. Guo, K. Liu, L. Liang, D. Zhang, Y. Liu and W. Zheng, *ACS Appl. Electron. Mater.*, 2022, **4**, 4653–4658.
- 3 D. Zhang, J. Liang, Z. Luo, Z. Wang, Y. Liu and W. Zheng, *IEEE Electron Device Lett.*, 2024, **45**, 168–171.
- 4 Q. Wang, P. Huang, Q. Liu, Y. Li, Q. Qu, M. Li, K. P. Homewood, Y. Lu and Y. He, *J. Alloys Compd.*, 2020, **834**, 155036.
- 5 C. Xu, L. Lan, Z. Wang, P. Lv and W. Zheng, *ACS Appl. Mater. Interfaces*, 2023, **15**, 12017–12023.